Journal of Composite Materials

http://jcm.sagepub.com

Experimental Study of Dynamic Crack Growth in Unidirectional Graphite/Epoxy Composites using Digital Image Correlation Method and High-speed Photography

Dongyeon Lee, Hareesh Tippur, Madhu Kirugulige and Phillip Bogert

Journal of Composite Materials 2009; 43; 2081 originally published online Jul 9, 2009;
DOI: 10.1177/0021998309342139

The online version of this article can be found at:
http://jcm.sagepub.com/cgi/content/abstract/43/19/2081

Published by:
SAGE
http://www.sagepublications.com

On behalf of:
American Society for Composites

Experimental Study of Dynamic Crack Growth in Unidirectional Graphite/Epoxy Composites using Digital Image Correlation Method and High-speed Photography

DONGYEON LEE, HAREESH TIPPUR* AND MADHU KIRUGULIGE
Department of Mechanical Engineering, Auburn University
Auburn, AL, USA

PHILLIP BOGERT
NASA Langley Research Center, Hampton, VA, USA

ABSTRACT: In this work, fracture behavior of multilayered unidirectional graphite/epoxy composite (T800/3900-2) materials is investigated. Rectangular coupons with a single-edged notch are studied under geometrically symmetric loading configurations and impact loading conditions. The notch orientation parallel to or at an angle to the fiber orientation is considered to produce mode-I or mixed-mode (mode-I and -II) fracture. Feasibility of studying stress-wave induced crack initiation and rapid crack growth in fiber-reinforced composites using the digital image correlation method and high-speed photography is demonstrated. Analysis of photographed random speckles on specimen surface provides information pertaining to crack growth history as well as surface deformations in the crack-tip vicinity. Measured deformation fields are used to estimate mixed-mode fracture parameters and examine the effect of fiber orientation (β) on crack initiation and growth behaviors. The samples show differences in fracture responses depending upon the orientation of fibers. The maximum crack speed observed is the highest for mode-I dominant conditions and it decreases with fiber orientation angle. With increasing fiber orientation angle, crack takes longer to attain the maximum speed upon initiation. Continuous reduction of dynamic stress intensity factors after crack initiation under mode-I conditions is attributed to crack bridging. The crack initiation toughness values decrease with the degree-of-anisotropy or increase with fiber orientation angle. A rather good agreement between crack initiation toughness values and the ones from previous investigations is observed. There is also a good experimental correlation between dynamic stress intensity factor and crack-tip velocity histories for shallow fiber orientations of $\beta = 0$, 15, and 30°.

*Author to whom correspondence should be addressed. E-mail: htippur@eng.auburn.edu
Figures 3–7, 9, 11 and 12 appear in color online: http://jcm.sagepub.com

0021-9983/09/19 2081–28 $10.00/0 DOI: 10.1177/0021998309342139

KEY WORDS: dynamic fracture, mixed-mode crack growth, fiber reinforced composites, optical metrology, digital speckle correlation, high-speed photography, stress intensity factors.

INTRODUCTION

GRAPHITE/EPOXY COMPOSITES are widely used in aerospace applications [1] for their excellent thermo-mechanical attributes. In view of the vast range of strain-rates this material encounters during service life, it is important to study and quantify mechanical performance of these materials in general and fracture behavior under elevated rates of loading in particular. In this study, primary focus is on stress-wave induced mixed-mode fast fracture in unidirectional graphite/epoxy coupons resulting from low velocity impact.

Mixed-mode deformations in unidirectional composites arise when (a) fibers are oriented at an angle in a specimen subjected to configurationally symmetric loading condition, (b) fibers are aligned relative to loading direction, but subjected to configurationally asymmetric loading, or (c) both. To date a number of studies on failure of fiber-reinforced composites under mixed loading are reported. Tirosh [2] studied energy release rate in unidirectional composites containing an inclined center crack parallel to fiber orientation. The crack was subjected to mixed-mode conditions in this study by loading at an angle with respect to fiber direction. Donaldson [3] also studied mixed-mode fracture of unidirectional graphite/epoxy system in order to establish a fracture envelope for the material. In this work, as the angle between the crack (parallel to fiber orientation) and loading axis decreased from 90° to 10°, mode-I critical stress intensity factor remained nearly constant, whereas mode-II counterpart increased exponentially. However, for angles <10°, both stress intensity factors drop abruptly. To the contrary, Seif and Shahjahun [4] used moiré interferometry to conclude that K_{Ic} increases continuously with increasing crack inclination angle whereas K_{IIc} increases up to 45° and then decreases. Unlike the aforementioned works, Liu et al. [5] created different mode mixities by employing a Brazilian disk geometry. They showed that normalized K_I decreased with increasing loading angle with respect to the crack, while K_{II} showed an opposite trend. Yum and Hong [6] theoretically examined mixed-mode fracture using collocation method to calculate stress intensity and geometric correction factors. In all these cases [2–6], the crack is oriented along the fiber direction.

When the pre-notch is not parallel to the fiber orientation (angle between fiber direction and crack direction), crack growth is characterized by noncoplanar crack initiation and kinked-crack propagation [7]. Parhizgar et al. [8] investigated effects of crack length and fiber orientation on fracture toughness of unidirectional composites. Using experiments and finite element simulations, they confirmed that composites with an angled pre-notch experienced both opening and sliding mode loadings. Further, an empirical formula relating fracture toughness and fiber orientation was reported. Rowlands [9] presented a relationship between fiber orientations for a multidirectional glass/epoxy system under cryogenic conditions. He reported an increase in K_I with increasing fiber orientation angle. A 3-fold increase was reported between fiber orientations of 0 and 15° followed by a much slower increase up to 45°. Sarkar and Maiti [10] related fracture toughness for an arbitrary fiber orientation with the one for zero degree orientation. They suggested three different relations based on stress criterion, Tsai-Hill criterion, and energy release rate criterion. All three criteria predicted K_{Ic} to increase with increasing fiber

orientation angle. In Tohgo et al. [7] and Suresh and Wang [11], instead of using conventional K_{I} and K_{II}, tensile and shear stress intensity factors, K_σ and K_τ, along the fiber direction were introduced. Interestingly, fracture toughness was shown to be uniquely described in K_σ–K_τ plane. Walker and Jamasri [12] took advantage of full-field displacement field measurements from a moiré interferometer in order to evaluate stress intensity factors in unidirectional graphite/epoxy composites under mixed-mode loading. They focused on only two fiber orientations, 75 and 90°, but showed that fiber orientation angle to be an important parameter affecting stress intensity factors.

From the above literature search it is clear that very few previous works have investigated stress-waves driven rapid crack growth in composites, particularly under mixed-mode (mode-I and -II) conditions. In the current work, dynamic crack growth behavior in unidirectional graphite/epoxy composites is studied optically. Transient crack growth is produced in edge notched sheet samples with different fiber orientations by impact loading. Fast fracture at crack velocities of several hundred meters per second is captured using a digital high-speed camera. The method of digital image correlation (DIC) [13,14] is employed in conjunction with high-speed photography to examine full-field surface-displacements in the vicinity of a rapidly growing crack. A relatively simple experimental set-up without the need for elaborate sample surface preparation (when compared to inteferometric methods) prompted the choice of DIC method. It is worth noting that in recent years DIC has become popular in the field of experimental mechanics [15–17]. Yet, due to the unavailability of ultra high-speed digital cameras capable of digitizing image intensities at relatively high spatial and temporal resolutions until quite recently, DIC has not been extensively used to study stress-wave induced failures in general and dynamic fracture mechanics of fiber reinforced composites in particular. The modern high-speed digital recording devices have also alleviated the artifacts associated with scanning of recorded photographic films obtained from traditional rotating mirror cameras. Accordingly, this work introduces novelty in terms of extending DIC to study dynamic fracture mechanics of fiber-reinforced composites using real-time high-speed imaging.

In the ensuing section, governing expressions for displacement fields in the vicinity of the crack-tip will be reviewed. Section 'Digital Image Correlation' is devoted for describing the experimental methodology employed in this study; its basic concept and the approach, experimental procedure and set-up in brief. Section 'Test Results' covers results and is followed by the issues concerning the validity of the developed method discussed in section 'Discussion'. In this section, the experimental results are analyzed and compared to the results from existing literature. In the final section, major conclusions of the work are outlined.

DISPLACEMENT FIELD OF ANISOTROPIC MATERIAL

The displacement components u and v in the vicinity of crack-tip due to mixed-mode (mode-I and mode-II) loadings are expressed as follows [18]:

$$\begin{aligned} u &= K_I\sqrt{\frac{2r}{\pi}}\mathrm{Re}\left[\frac{1}{\mu_2-\mu_1}(p_1\mu_2 z_1 - p_2\mu_1 z_2)\right] + K_{II}\sqrt{\frac{2r}{\pi}}\mathrm{Re}\left[\frac{1}{\mu_2-\mu_1}(p_1 z_1 - p_2 z_2)\right] + \cdots \\ v &= K_I\sqrt{\frac{2r}{\pi}}\mathrm{Re}\left[\frac{1}{\mu_2-\mu_1}(q_1\mu_2 z_1 - q_2\mu_1 z_2)\right] + K_{II}\sqrt{\frac{2r}{\pi}}\mathrm{Re}\left[\frac{1}{\mu_2-\mu_1}(q_1 z_1 - q_2 z_2)\right] + \cdots \end{aligned} \tag{1}$$

where quantities p_j, q_j, and z_j ($j=1, 2$) are defined as:

$$p_j = \mu_j^2 s_{11} + s_{12} - \mu_j s_{16}$$
$$q_j = \mu_j s_{12} + \frac{s_{22}}{\mu_j} - s_{26}$$
$$z_j = \sqrt{\cos\theta + \mu_j \sin\theta}$$

μ_j ($j=1, 2$) are the two roots of the following characteristic equation:

$$s_{11}\mu^4 - 2s_{16}\mu^3 + (2s_{12} + s_{66})\mu^2 - 2s_{26}\mu + s_{22} = 0 \tag{2}$$

with *positive imaginary part* and s_{ij} ($i, j=1, \ldots, 6$) are the elements of compliance matrix such that:

$$\begin{bmatrix} \varepsilon_{xx} \\ \varepsilon_{yy} \\ \varepsilon_{zz} \\ \gamma_{yz} \\ \gamma_{zx} \\ \gamma_{xy} \end{bmatrix} = \begin{bmatrix} s_{11} & s_{12} & s_{13} & s_{14} & s_{15} & s_{16} \\ s_{21} & s_{22} & s_{23} & s_{24} & s_{25} & s_{26} \\ s_{31} & s_{32} & s_{33} & s_{34} & s_{35} & s_{36} \\ s_{41} & s_{42} & s_{43} & s_{44} & s_{45} & s_{46} \\ s_{51} & s_{52} & s_{53} & s_{54} & s_{55} & s_{56} \\ s_{61} & s_{62} & s_{63} & s_{64} & s_{65} & s_{66} \end{bmatrix} \begin{bmatrix} \sigma_{xx} \\ \sigma_{yy} \\ \sigma_{zz} \\ \tau_{yz} \\ \tau_{zx} \\ \tau_{xy} \end{bmatrix} \tag{3}$$

Subscripts 1 and 2 denote the fiber direction and in-plane cross-fiber direction, respectively. The coordinates x and y are the two principal directions of a composite sample as illustrated in Figure 1. Here r is the radial distance from the crack-tip, θ the angle with respect to the x-axis, and β the fiber orientation angle.

Equations (1) can be further expanded to include transient effects associated with dynamic crack growth resulting from impact loading. For dynamic crack propagation under pure mode-I loading conditions, in-plane displacement components u, and v can

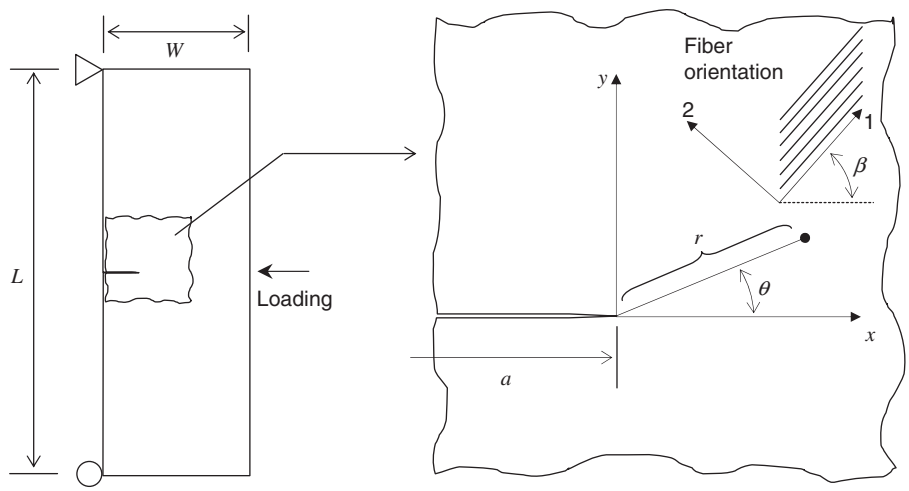

Figure 1. *Illustration of crack-tip neighborhood (L = 200 mm, W = 50 mm, a = 0.2 W).*

be rewritten as [19]:

$$
\begin{aligned}
u = \frac{K_{ID}}{\sqrt{\pi}} A c_{66} \Bigg[& -\left(\frac{l_1}{\alpha} s_{11} + p^2 l_3 s_{12}\right) \sqrt{\sqrt{\cos^2\theta + \frac{1}{p^2}\sin^2\theta} + \cos\theta} \\
& + \left(\frac{p l_2 l_5}{\alpha q l_6} s_{11} + \frac{p q l_4 l_5}{l_6} s_{12}\right) \sqrt{\sqrt{\cos^2\theta + \frac{1}{q^2}\sin^2\theta} + \cos\theta} \Bigg] \sqrt{r} + \cdots \\
v = \frac{K_{ID}}{\sqrt{\pi}} A c_{66} \Bigg[& -p\left(\frac{l_1}{\alpha} s_{12} + p^2 l_3 s_{22}\right) \sqrt{\sqrt{\cos^2\theta + \frac{1}{p^2}\sin^2\theta} - \cos\theta} \\
& + q\left(\frac{p l_2 l_5}{\alpha q l_6} s_{12} + \frac{p q l_4 l_5}{l_6} s_{22}\right) \sqrt{\sqrt{\cos^2\theta + \frac{1}{q^2}\sin^2\theta} - \cos\theta} \Bigg] \sqrt{r} + \cdots
\end{aligned}
\tag{4}
$$

where K_{ID} is dynamic stress intensity factor for mode-I.

The other parameters in Equation (4) are defined as follows [19,20]:

$$
\begin{cases} p = \sqrt{a_1 - \sqrt{a_1^2 - a_2}} \\ q = \sqrt{a_1 + \sqrt{a_1^2 - a_1}} \end{cases}
\qquad
\begin{cases} 2a_1 = \alpha + \alpha_1 - 4\beta\beta_1 \\ a_2 = \alpha\alpha_1 \end{cases}
$$

$$
A c_{66} = \frac{l_6}{p q l_4 l_5 - p^2 l_3 l_6}
$$

$$
\begin{cases} \alpha = \dfrac{c_{66}}{c_{11}(1 - M_1^2)} \\ \alpha_1 = \dfrac{c_{22}}{c_{66}(1 - M_2^2)} \end{cases}
\qquad
\begin{cases} 2\beta = \dfrac{c_{12} + c_{66}}{c_{11}(1 - M_1^2)} \\ 2\beta_1 = \dfrac{c_{12} + c_{66}}{c_{66}(1 - M_2^2)} \end{cases}
$$

$$
\begin{cases} M_1 = \dfrac{c}{c_l} \\ M_2 = \dfrac{c}{c_s} \end{cases}
\qquad
\begin{cases} c_l = \sqrt{\dfrac{c_{11}}{\rho}} \\ c_s = \sqrt{\dfrac{c_{66}}{\rho}} \end{cases}
\tag{5}
$$

$$
\begin{cases}
l_1 = \dfrac{2\beta p^2}{(\alpha - p^2)(1 - M_1^2)} + 2\beta - \alpha \\
l_2 = \dfrac{2\beta q^2}{(\alpha - q^2)(1 - M_1^2)} + 2\beta - \alpha \\
l_3 = 1 - M_2^2 - \dfrac{2\beta}{\alpha - p^2} \\
l_4 = 1 - M_2^2 - \dfrac{2\beta}{\alpha - q^2} \\
l_5 = -l_3 - M_2^2 \\
l_6 = -l_4 - M_2^2
\end{cases}
$$

in which c_{ij} ($i, j = 1, \ldots, 6$) are the elements of stiffness matrix, M_1 and M_2 the Mach numbers, c_l the longitudinal wave speed, c_s the shear wave speed, c the crack-tip velocity, and ρ the material density.

It must be noted that displacement fields in Equation (4) are valid for mode-I loading only and mixed-mode counterparts are unavailable at the moment. Further discussion on this issue will be presented later on.

DIGITAL IMAGE CORRELATION

Approach

In the DIC technique, random speckles on a specimen surface were monitored during a fracture event. The light intensity of speckle patterns was photographed before and after deformation. Deformed images corresponding to the fracture event were paired with the ones prior to loading. Each pair of images was analyzed separately. During the analysis, a sub-image within the undeformed image was chosen, and its counterpart in the deformed image was sought. Once the same location of a sub-image in the deformed image was identified, the local displacements could be readily quantified. In the current work, a three-step approach developed at Auburn [13,14] as an in-house software suite on a MATLAB^{TM} platform, was used to estimate in-plane 2D displacement components:

Step-1. Initial estimation of displacements: First, a 2D cross-correlation between the two selected sub-images was carried out. The peak of the correlation function was detected to an accuracy of 1/16 of a pixel using bicubic interpolation. This process was repeated for the entire image until full-field in-plane displacements were obtained over an array of grid points. Following Chen et al. [21], displacement fields u and v were obtained. After obtaining u and v displacements for a given sub-image, detecting the spatial location of the peak can be done with good accuracy. At this stage, however, displacement field contained significant random noise.

Step-2. Nonlinear optimization: In order to improve displacement fields obtained previously, an iterative approach was used to minimize the 2D correlation coefficient by using a nonlinear least-squares minimization technique. Initially, minimization was carried out in a two-variable space (*viz*., u-v space) by using the initial findings from Step-1. Next, minimization was carried out in a six-variable space (*viz*., u, and v as well as their four gradient components, $\partial u/\partial x, \partial u/\partial y, \partial v/\partial x$) by using values that are obtained previously. In this step, a significant amount of noise present in the earlier estimation was removed from the u and v fields.

Step-3. Smoothing crack-tip displacements: To further improve displacement fields, a smoothing algorithm was applied to (u, v) displacement fields separately. While doing so, the displacements were kept discontinuous across the two crack faces since upper part and lower parts undergo different deformations. The smoothing process employed in the present work allowed discontinuity of displacements across the crack faces. The data corresponding to the crack faces were excluded from the smoothing operation to preserve displacement discontinuity across the crack faces.

The smoothing method in the current work employed an unbiased optimum smoothing parameter based on the noise level present in the displacement field. Let l and m denote

displacement fields obtained from Step-2 and the one to be restored, respectively. Then an image can be represented in a vector-matrix form as:

$$l = H \cdot m + \eta \tag{6}$$

in which H represents the point spread function (PSF) and η the noise vector. Since the purpose of this step is to minimize η, one may evaluate either the inverse or pseudo-inverse of Equation (6). In many cases, however, matrix H is ill-posed (eigenvalues of this matrix are close to zero and hence too unstable for matrix inversion). This problem can be overcome by introducing a regularization term [22]. Instead of minimizing $\|l - Hm\|^2$, one should minimize

$$\|l - Hm\|^2 + \alpha_s \|Lm\|^2 \tag{7}$$

in order to estimate m. Here $\| \ \|^2$ is the Euclidean vector norm ($\|f\|^2 = f^{\mathrm{T}} f$), L denotes 2D Laplacian operator, and α_s is the regularization parameter selected on the basis of the noise present in the displacement field. The parameter α_s controls smoothness of a restored image. High α_s is required if the noise variance is high or H is highly ill-posed. However, a large value of α_s may create an excessively smooth image. Therefore, an optimum value of α_s must be chosen. In the current work, smoothing parameter α_s was chosen so that data infidelity satisfied the condition [23]:

$$\sigma^2 = \frac{1}{n} \sum_{j=1}^{n} [m(j) - l(j)]^2 \tag{8}$$

where n is the total number of data points and σ^2 is the variance of the noise present in the displacement field.

Differentiating Equation (7) with respect to m and equating the result to zero yields a restored image, m, as follows:

$$m = \left(H^{\mathrm{T}} H + \alpha_s L^{\mathrm{T}} L\right)^{-1} H^{\mathrm{T}} l \tag{9}$$

The restored displacement field is often disguised by noise and high-frequency artifacts. Such artifacts and noise can be filtered by using a Laplacian filter kernel as:

$$L(x, y) = \begin{bmatrix} 0 & 1 & 0 \\ 1 & -4 & 1 \\ 0 & 1 & 0 \end{bmatrix} \tag{10}$$

The Laplacian kernel is imposed over a 3×3 array of original pixels in a restored field, and each pixel is multiplied by the corresponding value in the kernel in Equation (10). The nine resulting values are summed and the resulting value for the filter kernel is added to the (2,2) element in that 3×3 data array, and this newly created number replaces the original digit of the central pixel. This process is repeated for all pixels over the entire image except the outermost columns and rows. The new array represents the filtered field.

A result from the aforementioned three-step approach is shown in Figure 2. A typical case of a displacement field in the y-direction is shown as an example. As seen in this figure, contours are relatively discontinuous due to random noise scattered over the entire

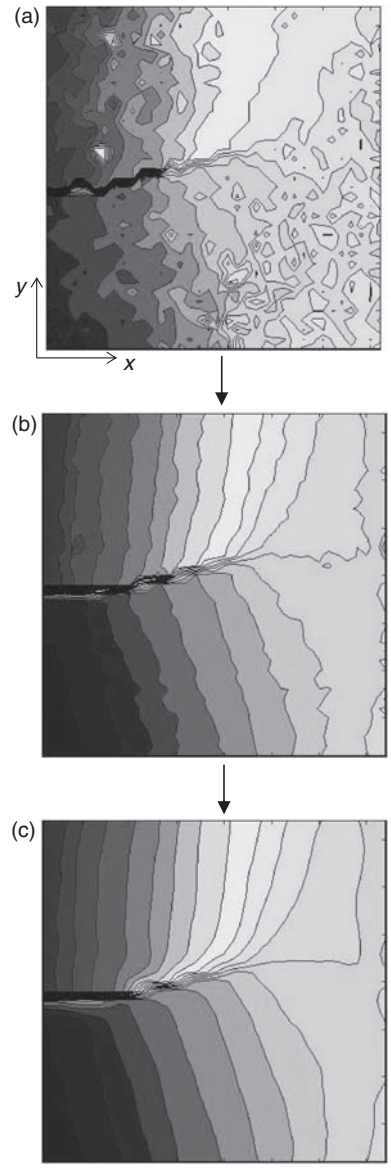

Figure 2. *Example of the three-step – (a) Step #1, (b) Step #2, (c) Step #3 – DIC methodology for refining displacement fields (for $\beta = 15^{\circ}$ case and displacements in the y-direction).*

area after Step-1 (Figure 2(a)). After Step-2, noise is noticeably reduced, but still the contours are not as smooth as one would expect (Figure 2(b)) for a material continuum. Following Step-3 contour lines become relatively free of noise and can be readily used (Figure 2(c)) in an analysis. Although the contours in the vicinity of crack faces are distorted, they do not affect the estimation of fracture parameters since regions close to the crack-tip and crack flanks are generally excluded from the analysis using 2D fracture mechanics theories.

Sample Preparation

Composite panels were fabricated from T800/3900-2 (Toray Composite America, Inc.) prepreg tapes by hot-compression molding. A total of 35 plies were stacked together, resulting in 6.2-mm thickness, with fibers aligned in one direction. Panels were cut into $200 \times 50\,\text{mm}^2$ rectangular coupons with four different fiber orientations, 0, 15, 30, and 45°, relative to the width of specimens. The material properties are listed in Table 1, in which subscripts 1 and 2 represent directions parallel and perpendicular to the fiber orientation, respectively (Figure 1). For different angled configurations considered, elastic moduli and Poisson's ratio were computed by rotational transformations and are listed in Table 2.

Each specimen was then pre-notched with a 0.3-mm thick diamond wafer blade. A razor blade was used to further sharpen the notch tip into a crack. The initial pre-notch of length 10 mm was along the line-of-symmetry at the sample edge and oriented along the impacting direction. The fiber alignment relative to the pre-notch determines fiber orientation angle β, as shown in Figure 1. Pre-notched samples were then sprayed with mists of black and white paints alternatively to create fine random speckles.

Testing Procedure

A schematic of the experimental set-up is shown in Figure 3. It consisted of an Instron-Dynatup 9250-HV drop tower for delivering low-velocity impact and a Cordin-550

Table 1. Material properties of T800/3900-2 composite.

	In-house measurement	Manufacturer's nominal values	Values used in this study
Modulus[a]			
E_1	171.6[b]	170.0	171.6
E_2	8.25[b]	8.5	8.25
G_{12}	6.21[b]	–	6.21
Poisson's ratio			
ν_{12}	0.344	0.34	0.344

[a]*E* and *G* in Gpa.
[b]Provided by NASA.

Table 2. Material properties of T800/3900-2 composite for nonzero β.

	$\beta = 0°$	$\beta = 15°$	$\beta = 30°$	$\beta = 45°$
Modulus (GPa)				
E_{xx}	171.6	64.77	24.80	14.08
E_{yy}	8.25	8.67	10.20	14.08
G_{xy}	6.21	6.51	7.22	7.63
Poisson's ratio				
ν_{xy}	0.344	0.252	0.190	0.134
Wave speed (m/s)[a]				
c_l	10480	9840	8120	5840
c_s	1980	3130	4650	5250

[a]Longitudinal and shear wave speeds are computed by Equation (5).
Material density (ρ) = 1580 kg/m^3.

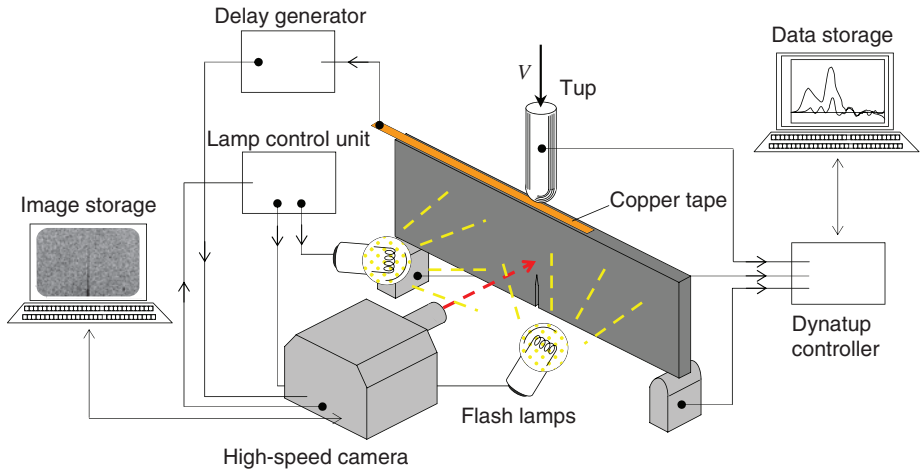

Figure 3. *Schematic of the experimental setup used.*

high-speed digital camera[1] for capturing speckle images in real-time. The drop tower had an instrumented tup for recording the impact force history and a pair of anvils for recording support reaction histories. The set-up also included a delay generator to generate a trigger pulse when the tup contacted the specimen. Since all images were recorded during the dynamic event lasting less than 200 μs, two high-intensity flash lamps, triggered by the camera, were used to illuminate the specimen surface. Two separate computers were used – one for recording the impact force and anvil reaction histories and the other for controlling the high-speed camera and storing digitized images.

The high-speed camera used a combination of CCD-based imaging technology and a high-speed rotating mirror optical system. It is capable of capturing 2,000,000 frames per second at a resolution of 1000×1000 pixels per image. It is equipped with 32 independent image sensors positioned circumferentially around a five-facet rotating mirror, which reflects and sweeps light over the sensors (Figure 4). Each sensor is illuminated by a separate optical relay circuit containing separate lenses and partial mirrors. That is, there are 32 individual cameras operating sequentially by means of internal electronic triggering. Accordingly, minor misalignments such as differences in focus and rotational discrepancies between any two consecutive images are to be expected. These misalignments preclude correlation of images recorded by two different sensors. This, however, can be resolved by 'pairing' images such that each pair consists of an undeformed and a deformed images recorded by the *same* sensor (and its optical relay). This was accomplished as follows: prior to impacting the specimen, a set of 32 images of the region-of-interest was photographed at a desired framing rate (250,000 frames per second in the current work). After aligning the optics, the rotating mirror was brought to the desired speed. The camera and flash lamps were triggered externally by the operator. This produced a set of 32 images of the specimen surface, one per sensor, and then all images were stored. While maintaining all camera settings (framing rate, focal distance, etc.) unchanged, a second set of 32 images was photographed as the specimen was subjected to impact loading. During the

[1]Details pertaining to camera calibration for digital image correlation can be found in Kirugulige and Tippur [14].

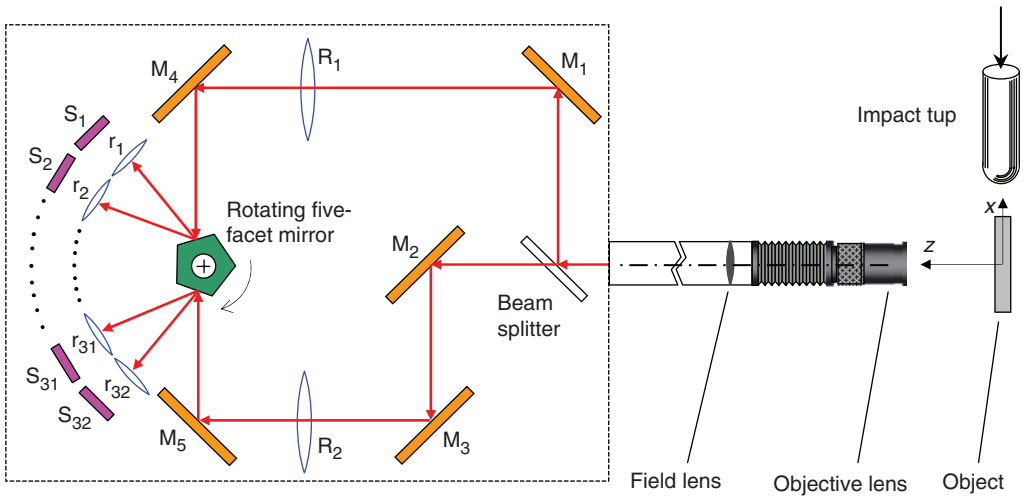

Figure 4. *Schematic illustration of the high-speed camera used: $M_1, \ldots, M_5$ indicate mirrors; R_1 and R_2 the relay lenses; $r_1, r_2, \ldots, r_{32}$ the relay lenses for CCDs; $S_1, S_2, \ldots, S_{32}$ the CCD sensors.*

second recording, the camera and flash lamps were triggered by the tup as it made contact with an adhesively backed copper strip attached to the top edge of the sample. Thus, for every image in the deformed image set, there was a corresponding image in the undeformed set. After identifying the first image photographed for undeformed and deformed sets, the corresponding two images from each set were paired. Each of these 32 matched pairs was analyzed separately. In this work, impact speed was set at 4.8 m/s.

TEST RESULTS

A few selected speckle images with corresponding displacement fields are shown in Figure 5. In this case fiber orientation angle β is 45°. Dynamic crack growth along the fibers is visible in these images and the crack-tip is shown by an arrow in the figure. The speckle images were analyzed using an in-house MATLAB^{TM} code [13,14]. In this work, displacements were generated as a matrix of 37×37 points over the entire area for every pair of images. From the displacement matrices the in-plane displacement contour plots were obtained for each time step. The corresponding crack opening displacement, v (displacement along the y-axis or in the vertical direction), and sliding displacement, u (displacement along the x-axis or in the horizontal direction), for the images are also shown in Figure 5. The discontinuity in displacements is evident across the crack faces in each image. Also, following crack initiation, contour lines of u show a set of isolines emergent from the right-hand side of the image. These are due to the impact occurring on the edge of the sample opposite to the crack-tip. One speckle image and the corresponding displacement fields for each of the other fiber orientation angles (0, 15 and 30°) are also shown in Figure 6 for the sake of completeness. Each of these images in this figure corresponds to a situation during crack propagation. Evidently, displacement fields estimated for $\beta = 0°$ case, show symmetry relative to the crack plane. The accuracy of displacement measurements in all these is ~1.4 μm as detailed in Kirugulige and Tippur [14].

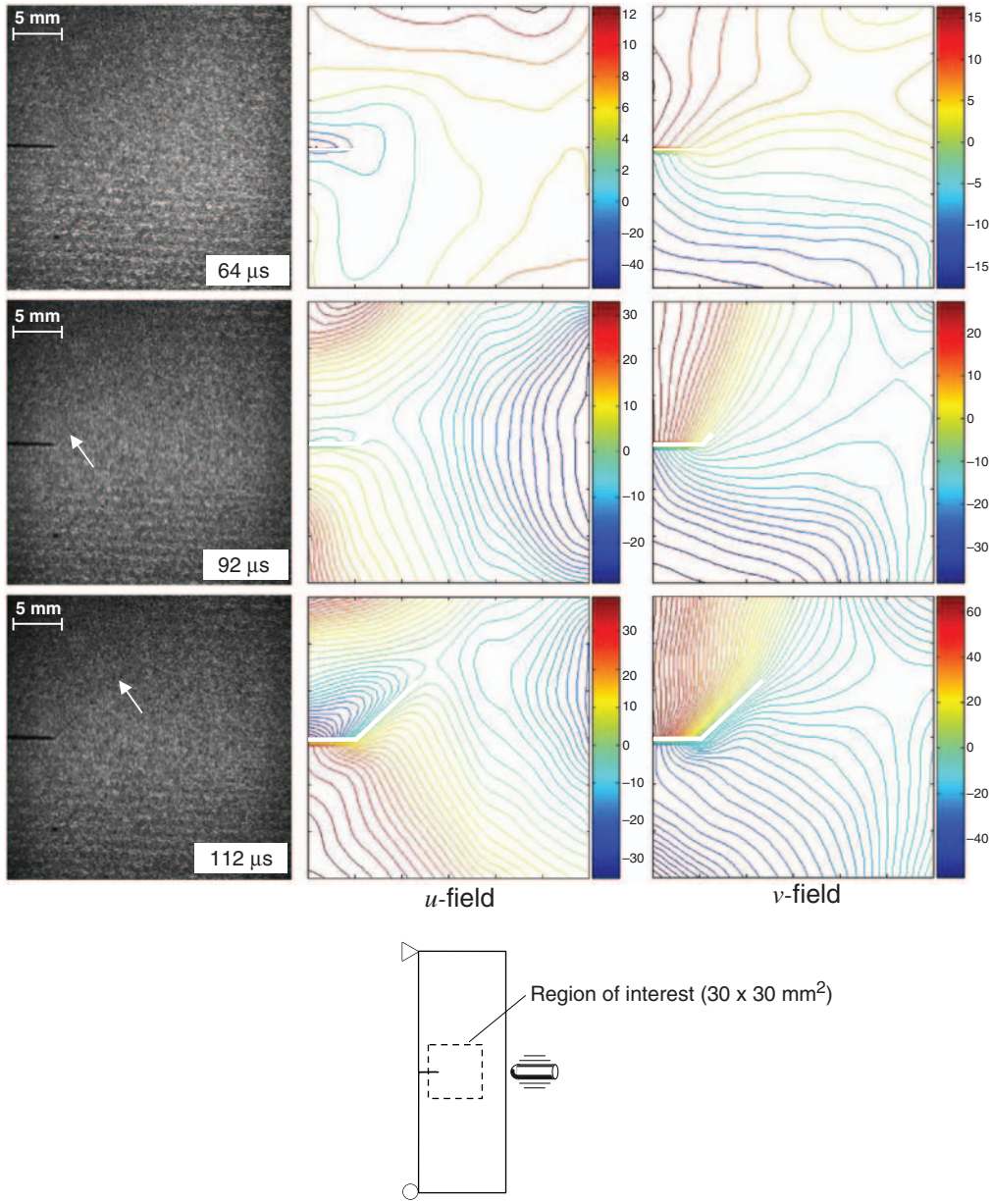

Figure 5. *Representative speckle images for $\beta = 45^\circ$ case ($30 \times 30\,mm^2$) with full-field sliding (u; second column) and opening (v; third column) displacement contours (crack initiation takes place at $t \sim 84\,\mu s$). Moving crack-tip is indicated by an arrow and the dark line is the initial crack in photographed images. Tick interval in the axes of displacement fields is 5 mm. Color-bar indicates displacement in micrometers. Contour interval here is 2 μm.*

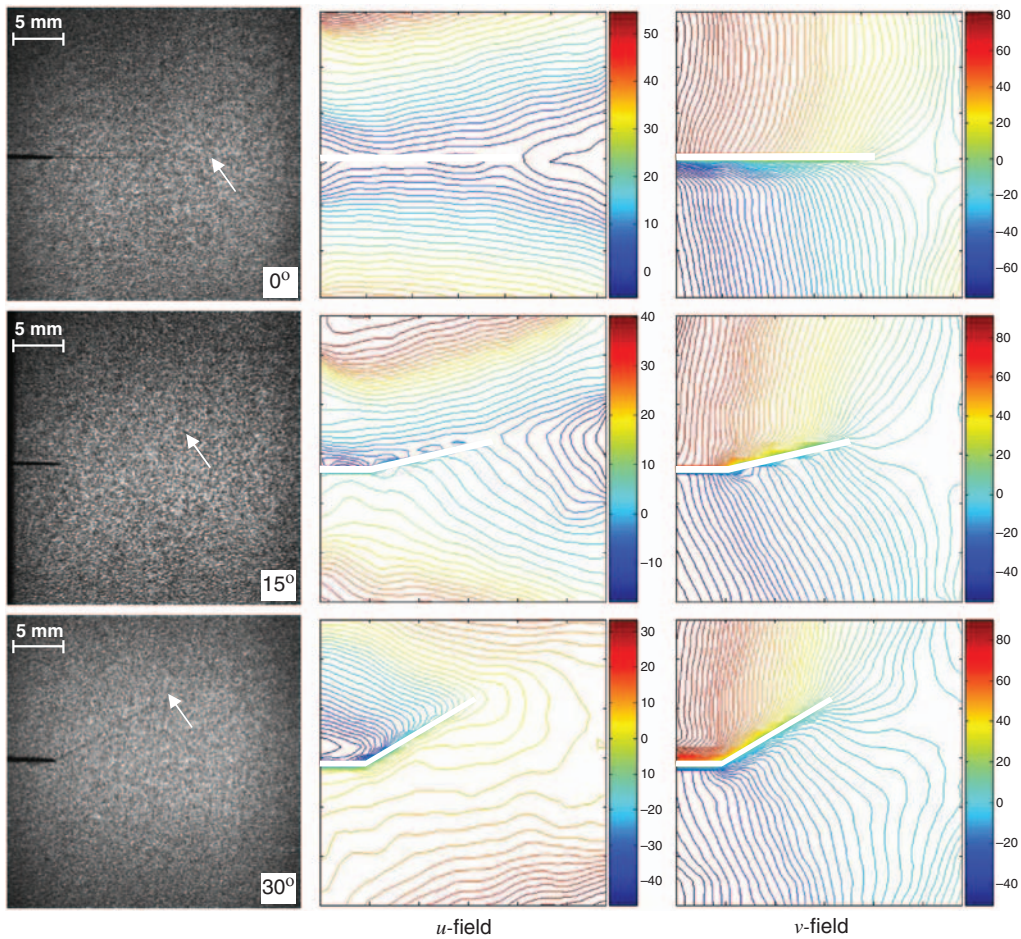

Figure 6. *Representative speckle images for $\beta = 0^\circ$, $\beta = 15^\circ$, and $\beta = 30^\circ$ ($30 \times 30\,mm^2$) with full-field sliding (u; second column) and opening (v; third column) displacement contours. All images were photographed 28 μs after crack initiation. Moving crack-tip is indicated by an arrow and the dark horizontal line is the initial crack in photographed images. Tick interval in the axes of displacement fields is 5 mm. Color-bar indicates displacement in micrometers. Contour interval here is 2 μm.*

These displacement values are used next along with Equation (1) to compute stress intensity factors.

As noted in Yoneyama et al. [24], locating the current crack-tip from the recorded image is difficult and needs particular attention. Precise location of a stationary or moving crack-tip is important for determining crack growth and stress intensity factor histories accurately. In this work, photographed images and aforementioned displacement matrices were consulted simultaneously for this purpose. Details on the process will be discussed in the next section.

For all available angles, the crack length is plotted against time in Figure 7. In each case a monotonic crack growth in the window of observation is evident. Here $t = 0$ indicates the instant the impactor head makes contact with the specimen. From these plots, the (initial) slopes for each angle are distinguishable from one another. Although determining the

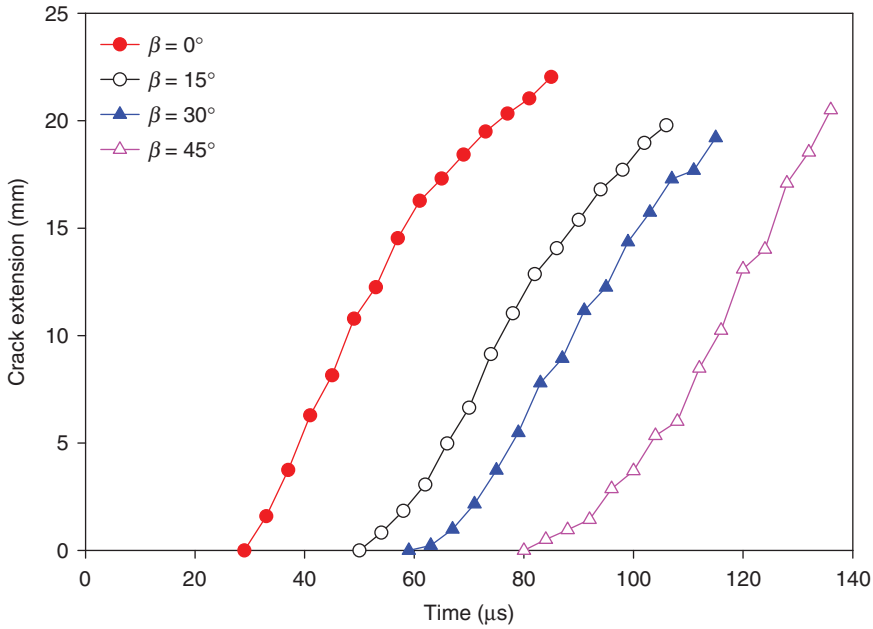

Figure 7. *Crack growth history against time for dynamic loading case. Initial slopes are ~510, 370, 310, 220 (m/s) for $\beta = 0$, 15, 30, 45°, respectively. Error bars indicate typical standard deviations computed from three different crack-tip locations (see section 'Discussion' for details).*

initial slope from these crack length histories depends on the number of selected data points, best estimates are 510, 370, 310, 220 (m/s) for $\beta = 0$, 15, 30, 45°, respectively as listed in Figure 7. A gradual reduction in the initial crack velocity with increasing fiber orientation is evident. The crack-tip velocity histories are also computed from the crack length history data for each case. Before computing velocity, each data set was smoothed using a cubic Bezier curve with a smoothing parameter of 0.5 (0.5 was chosen because it was desired that a smoothed data point should be located midway from a data point to an adjacent point). The crack-tip velocities were determined from the fitted curves. The results for each angle are shown in Figure 8 along with the respective crack length data and the fitted curves.

A maximum velocity for each case is in the range of 460–560 m/s, with the highest velocity in the case of $\beta = 0°$. The velocity variations in each case are shown in Figure 8. As the fiber orientation increases (from Figure 8(a) to (d)), the peak of velocity curves occurs earlier for $\beta = 0°$, and progressively later for 15, 30, and 45°. This can be explained in terms of increasing shear deformations with fiber orientation. For a pre-notch that is noncollinear with fiber orientation, a significant portion of the accumulated energy at the crack-tip is consumed by the crack initiation due to bridging of fibers across the crack flanks. In view of this, even after crack initiation, it takes relatively longer time to reach the maximum velocity for higher β values. Furthermore, following crack initiation, the crack-tip velocity in each case continues to increase monotonically for longer durations with increasing fiber orientation: the shortest duration is for the 0° case and the longest for the 45° case. Once the crack has attained the peak velocity, a decreasing trend exists due to increasing shear component as well as the compression dominated impact region.

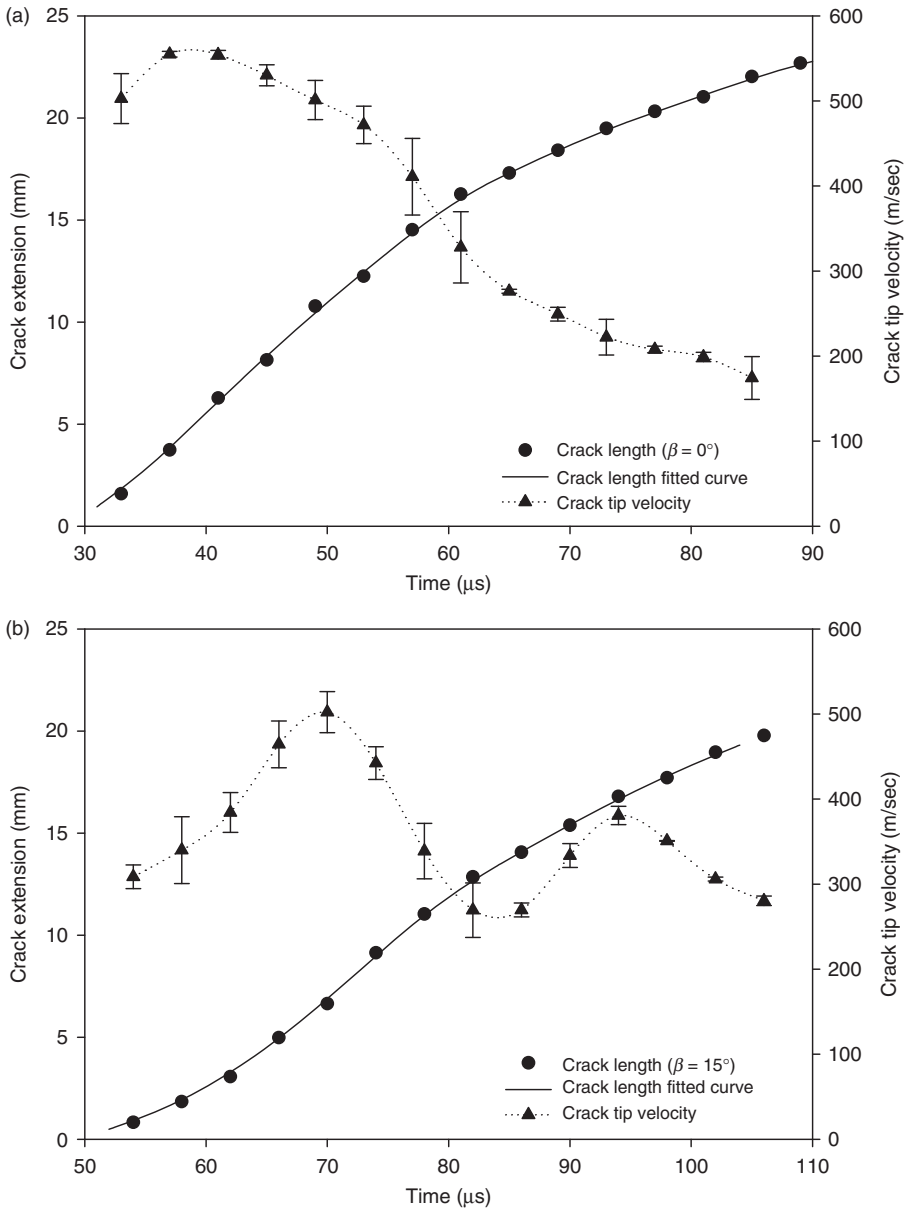

Figure 8. *Crack growth behavior in each angle configuration in comparison with crack-tip velocity: (a) $\beta = 0°$, (b) $\beta = 15°$, (c) $\beta = 30°$, (d) $\beta = 45°$.*

DISCUSSION

Selection of Displacement Field for Fracture Parameter Estimation

Measured displacement fields were used to estimate stress intensity factors. Since complex 3D deformations occur very close to the crack-tip, Equation (1) cannot satisfactorily

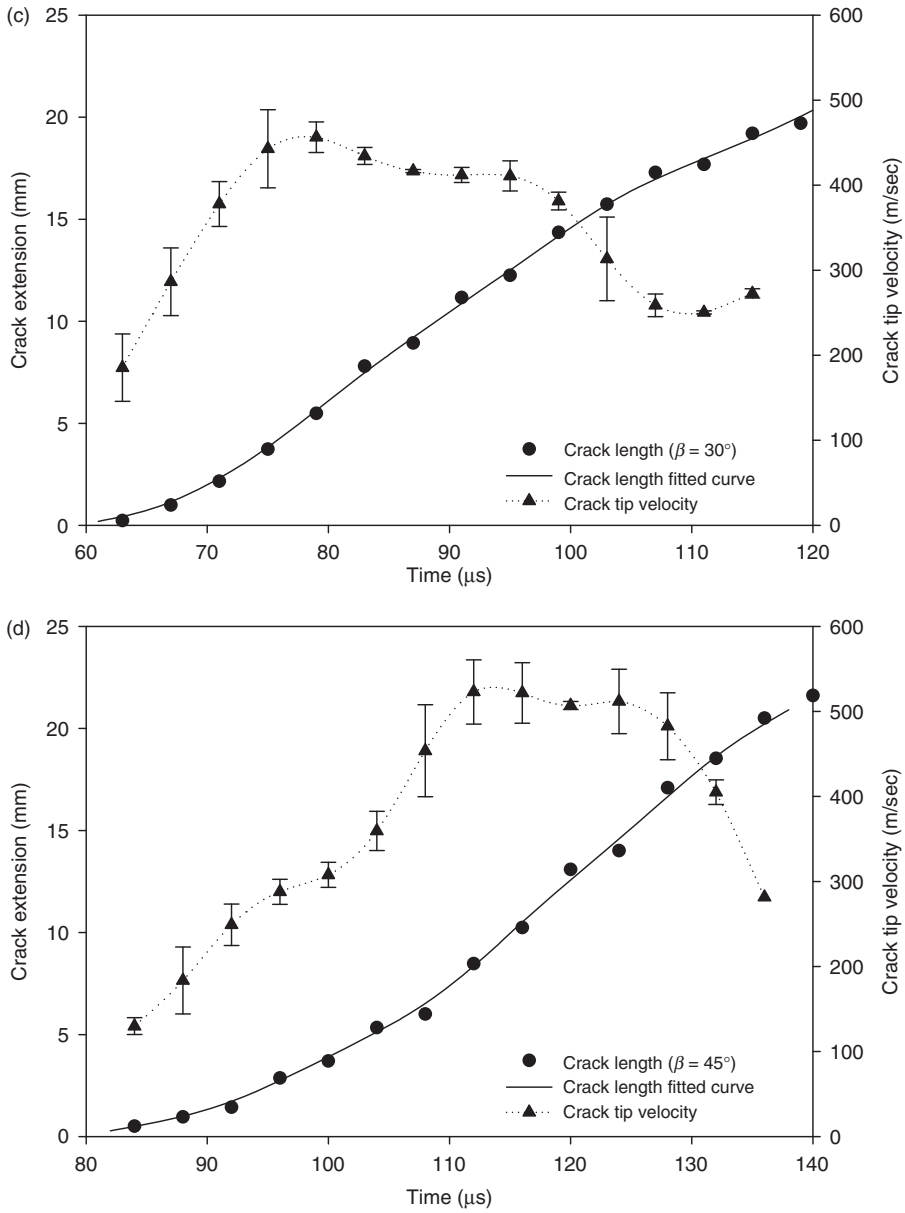

Figure 8. *Continued.*

represent 2D displacements, and hence data in the domain $r/B < 0.5$ (B being sheet thickness) were excluded from analysis. Data points in the vicinity of the crack were selected radially with respect to the crack-tip, and then were analyzed using an over-deterministic least-squares analysis [13,25].

Ideally, stress intensity factors can be evaluated using any of the two measured displacement components u_x (u as in Equation (1)) and u_y (v as in Equation (1)), or using

transformed components in polar coordinates, namely radial (u_r) and tangential (u_θ) displacements. Stress intensity factor histories obtained for $\beta = 0^\circ$ (mode-I) case from all these four displacement components used individually are shown in Figure 9(a). Also shown in the figure are the values of mode-I stress intensity factors obtained from an elasto-dynamic finite element computation[2] performed up to the observed crack initiation time. In Figure 9(b) the corresponding measured impact force histories used in the computations as boundary conditions are shown. The crack initiation occurs in this case at approximately 33 μs after impact. Evidently, the values obtained from opening (u_y) and radial (u_r) displacement fields are in close agreement with the computed ones with the latter having closer agreement as crack initiation time approaches. On the other hand, the values from u_x field are significantly lower than the computed values and oscillate in an unpredictable manner. The values obtained from tangential displacement over-predict the computed values.

The advantages of using radial and tangential displacements instead of the traditional Cartesian displacement components to determine mixed-mode stress intensity factors has also been demonstrated in the previous works of Yoneyama et al. [24] and Kirugulige and Tippur [14]. In the latter, it has been further demonstrated that radial displacement field offers additional robustness over tangential components. They have shown that the leading term in the asymptotic expression for radial displacement component should be sufficient for estimating crack-tip stress intensity factors accurately using over-deterministic least-squares analysis. In view of these, stress intensity factors presented hereafter were obtained from radial displacement field unless stated otherwise.

Locating the Crack-tip

To locate the moving crack-tip in the photographed images, both the image and displacement fields were consulted. The crack-tip in the photographed images was first identified by narrowing down its location to a few pixels. Then the fact that a crack is punctuated by a discontinuity or 'jump' in values of displacements across its faces was used. If the values jump from one sub-image to the adjacent in this region, the next row (or column) was considered sequentially until no evidence of jump was detected. One cell in the matrix was approximately equal to $0.85 \times 0.85\,\text{mm}^2$. Therefore possible error in locating the moving crack-tip is ± 0.43 mm.

To further clarify the error associated with the process of locating the crack-tip on stress intensity factors, K_I and K_II, were evaluated based on three different locations – a point identified as the *apparent* crack-tip (point b in Figure 11 inset), another 0.43 mm ahead of the crack-tip (point c), and the other 0.43 mm behind the crack-tip (point a). Thus obtained results for $\beta = 0^\circ$ case are shown in Figure 10. It should be noted that since the crack-tip location before crack initiation is identifiable with relative ease, error margin is reduced to 0.2 mm in the pre-initiation images. Hence the associated error in stress intensity factors prior to crack initiation is relatively small. However, errors increase after crack initiation particularly for the crack-tip location at point c. A similar trend was

[2]The dynamic simulations were performed in ANSYS structural analysis (v 10.0) environment. Plane stress explicit analysis involving 4026 elements and 4582 nodes with prescribed elastic properties (material density = $1580\,\text{kg/m}^3$) was employed. The measured force histories from the impact head and the support anvils were used as input boundary conditions. Further details are avoided here for brevity. The regression analysis of computed displacements was used to determine instantaneous stress intensity factors.

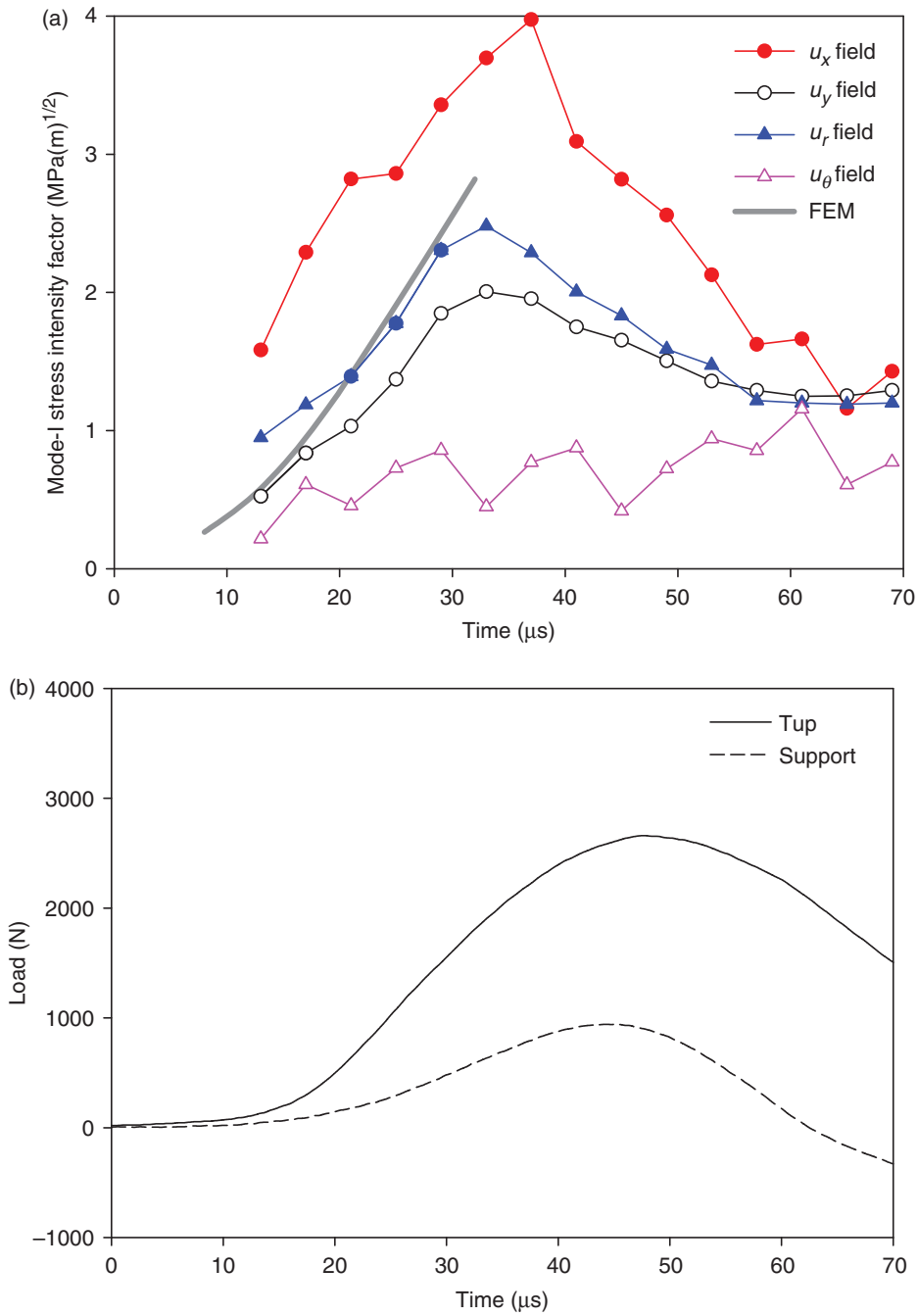

Figure 9. *Measured and computed stress intensity factor histories. (a) Comparison of K_I-values for $\beta = 0^\circ$ using different displacement fields and finite element method: time zero indicates impact time. (b) Load history of impact tup and one of two supporting anvils.*

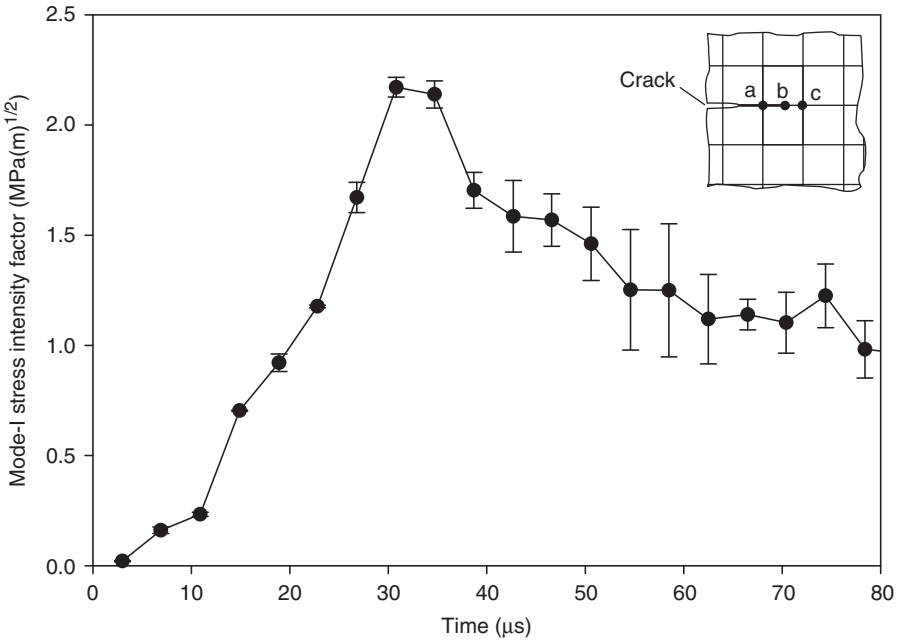

Figure 10. *Error estimation based on stress intensity factors for crack-tip locations a, b, and c. Point b is the apparent crack-tip.*

observed for other fiber orientation angles as well. In view of this, it can be concluded that caution should be exercised not to overestimate the crack length, whereas the effects of underestimation seem to be relatively benign. Uncertainty in locating the crack-tip can be mitigated in part by using a nonlinear least-squares method as in [24].

Effect of Crack Velocity

As noted earlier, quasi-static displacement fields, expressed in Equation (1), do not take into account effects of crack-tip velocity and only inertial effects are accounted for by the coefficients of the dominant crack-tip deformations as stress intensity factors. It should be noted, however, explicit asymptotic expressions for displacement fields that account for crack-tip velocity are not readily available for a mixed-mode case. Hence, velocity effects are examined for the mode-I ($\beta = 0^\circ$) situation only. The stress intensity factor histories obtained using Equation (4) are shown in Figure 11(a). Evidently the values obtained are very close to the one from Equation (1). Since the crack-tip velocity is the highest for $\beta = 0^\circ$, suffice it to say that the effect of velocity-dependent terms is rather small for angles other than $\beta = 0^\circ$. This observation can be used to conjecture that velocity effects are minimal in the current study. Thus, it can be argued that even for the mixed-mode cases in this study, Equation (1) are still useful for obtaining rather accurate estimates of stress intensity factors. However, this does not imply that velocity effects are generally negligible. This can be vividly demonstrated by introducing a range of velocities (500–1800 m/s) hypothetically into Equation (4) during least-squares analysis.

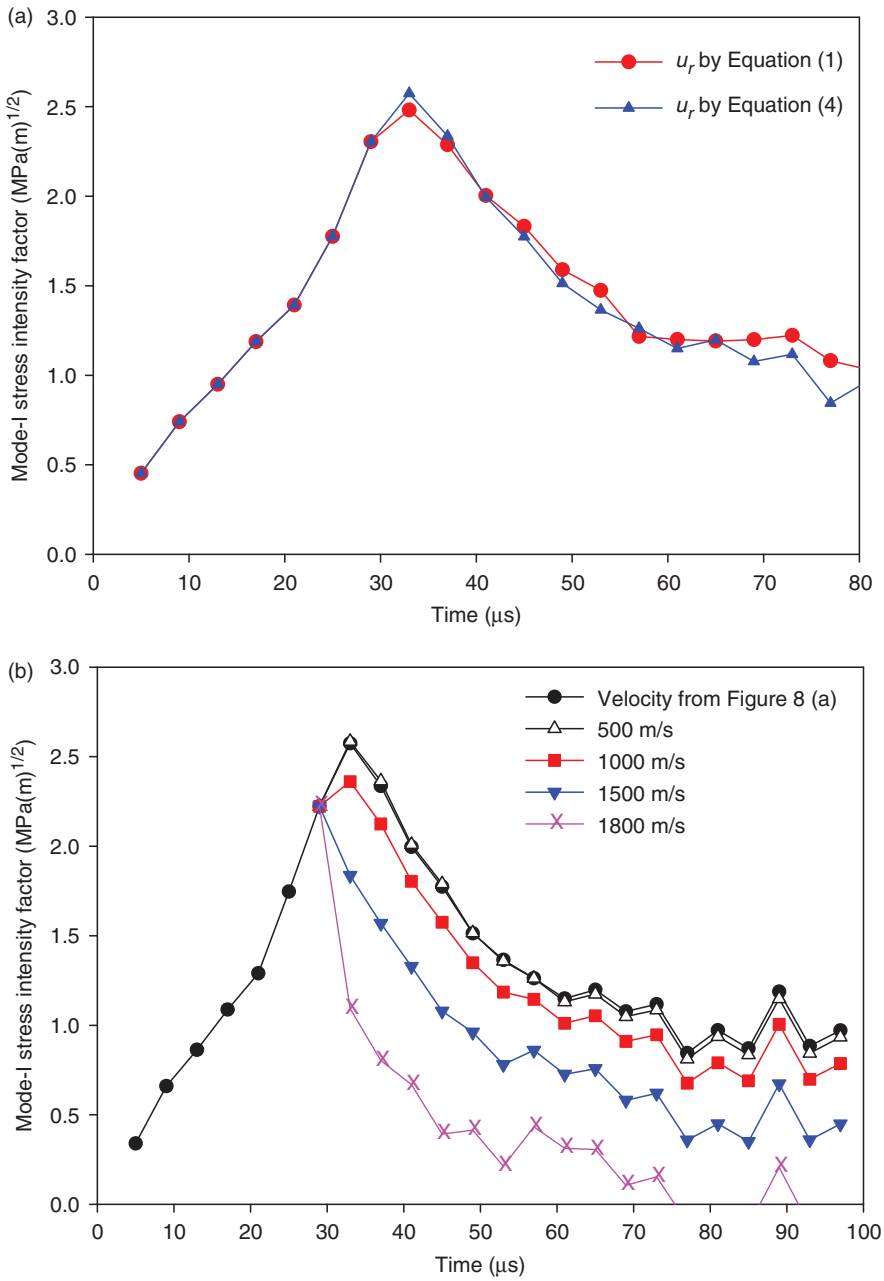

Figure 11. *Validity in the use of velocity independent displacement fields to determine stress intensity factor histories.*

Those results are shown in Figure 11(b). In these calculations, instead of using variable velocities as in the real experiment, input velocity is maintained constant at four different values during the analysis of data for time instances after crack initiation. Evidently high crack-tip velocity produces significant shifts in K_I histories. In this context, it is worth

noting that K_I value becomes a complex number if the input velocity is larger than 1980 m/s. That is, if the crack-tip velocity exceeds 1980 m/s, then the validity of Equation (4) is questionable. The velocity of 1980 m/s here is equal to the shear wave speed for the current material and $\beta = 0^\circ$. If the crack-tip velocity c is larger than c_s, then the Mach number M_2 $(=c/c_s)$ is greater than 1, implying that the crack growth is no longer subsonic, but intersonic (the term 'intersonic' is referred to the dynamic crack growth faster than the shear wave speed, but slower than the longitudinal wave speed). It was experimentally shown that intersonic crack growth would be impossible in orthotropic media under mode-I loading as suggested by Equation (4) resulting in a complex number. The issue on Intersonic crack propagation in composite materials is well documented in Huang et al. [26] and Coker and Rosakis [27].

As stated earlier, the results presented are based on *quasi-static* elastic properties. Although finding elastic properties for dynamic situation is beyond the scope of the current work, it may be helpful to examine the strain-rate sensitivity of a graphite/epoxy system in order to validate the current work. Gilat et al. [28] reported that a stiffer material response was detected in a graphite/epoxy system when strain rate was increased. Similarly, Daniel et al. [29] have also noted that unidirectional graphite/epoxy composites were strain-rate sensitive in terms of material properties. They have reported that E_1 changes by 6%, E_2 by 76%, while G_{12} and ν_{12} remain nearly strain rate independent when strain rate changes from $10^{-4}\,s^{-1}$ to approximately $20\,s^{-1}$.

In this context, a preliminary study was conducted to estimate the strain rates involved during the fracture process in the present work. This was done by mounting strain gages on specimens with two different fiber orientations of $\beta = 0^\circ$ and 45° and testing them under static and dynamic loading conditions (The strain gage methodology adopted here is based on the work of Khanna and Shukla [19], who have proposed a technique for determining fracture parameters. The details are avoided here for brevity). The strain signals from gages mounted at optimum angles and distance near the crack-tip were acquired in real time as the sample was subjected to loading. Using the acquired gage signals, the crack-tip strain rate was found to be in the range of $5\text{–}6 \times 10^{-5}\,s^{-1}$ for quasi-static tests and $50\text{–}70\,s^{-1}$ for high strain-rate ones. This matches the range of strain rates reported by Daniel et al. [29] reasonably well and hence it can be deduced that, except for transverse tensile modulus E_2, other elastic characteristics can be assumed to be relatively strain rate independent.[3] In this regard, material properties listed in Tables 1 and 2 can be claimed to be valid to a reasonable extent for a comparative study such as the one undertaken in this work. However, exact value of transverse tensile modulus would be more appropriate when a *true* value of stress intensity factor is needed.

Effects of Fiber Orientation Angle β

Stress intensity factors for all fiber orientations are presented against the time variable in Figure 12. The mode-I and -II stress intensity factor histories are shown in Figure 12(a), in which crack initiation times are self-evident by the peak points of K_I. Trends of K_I for all

[3]Although experimental methods as well as materials in [29] and in this work were not the same, it was postulated that the graphite/epoxy system in the current work would exhibit a similar change in the given range of strain rates.

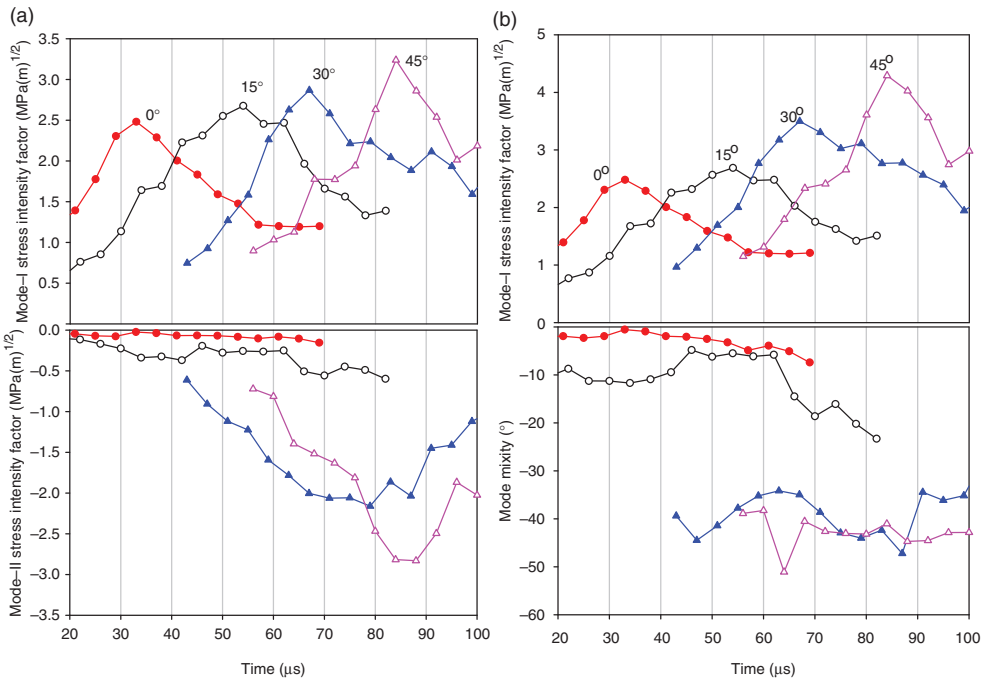

Figure 12. *Extracted stress intensity factors for various angles under dynamic loading condition: Mode-I and -II stress intensity factors (a) and effective stress intensity factor and mode mixity (b) against time.*

orientations are similar to each other – monotonic increase up to crack initiation, peak value at or near crack initiation, a continuous decrease following initiation. However, K_{II} trends are considerably different from those for K_{I}. Mode-II stress intensity factors for lower angles (*viz*., 0° and 15°) are nearly zero, whereas histories for higher angles (*viz*., 30° and 45°) exhibit significantly high values even prior to crack initiation. More interestingly, K_{I} at initiation increases with increase of angle in a linear fashion, whereas K_{II} at initiation increases exponentially. This exponential increase in K_{II} appears to be the main factor that brings out effects of fiber orientation. It is also interesting to note that, unlike isotropic materials, a nonzero K_{II} during crack propagation is possible during mixed-mode fracture of unidirectional composites.

In Figure 12(b), effective stress intensity factor (K_{eff}) histories for different fiber orientations are presented. The effective stress intensity factor is computed as $\sqrt{K_I^2 + K_{II}^2}$. In general, regardless of angles, effective stress intensity factors monotonically increase before crack initiation and attain a peak value at or near crack initiation time. A steady increase of K_{eff} can be explained by the increasing crack-tip loading up to the initiation event occurring no earlier than 30 μs after impact. More specifically, initial slope and the location of peak value are quite different from one another. K_{eff} values at crack initiation (close to the peak value of K_{eff} history) increase modestly from 0° to 15°, while they are much higher for higher angles. For lower β (namely, 0 and 15°), due to lower resistance against crack initiation along the fiber direction, crack initiation occurs earlier. On the other hand, for higher β (namely, 30 and 45°), crack initiation occurs much later after

impact due to noncollinear configuration. Crack initiation times for the four cases considered are 33, 54, 63, 84 μs for $\beta = 0$, 15, 30, and 45°, respectively. The magnitude of the stress intensity factor at crack initiation for different fiber orientation angles increases with increasing fiber orientation angle.[4]

Mode mixity (ψ), defined as $\tan^{-1}(K_{II}/K_I)$, histories are also plotted as a function of time for the four different angles. Within experimental errors and stress wave induced oscillations, the values of ψ are nearly constant in each case. More interestingly, in each case, mode-mixity does not exhibit any significant change upon crack initiation. This is unlike mixed-mode fracture of isotropic brittle materials (for example, see [14]) where mode-mixity values approach zero as the crack initiates and remains zero (within experimental accuracy) during crack growth in a direction normal to the local maximum tangential stress criterion (or, the $K_{II} = 0$ criterion). The magnitude of mode-mixity values for each angle also should be noticed. For the mode-I case, as expected, the values of mode-mixity remain close to zero (the deviation from zero is an indicator of the degree of accuracy in the estimation process). When the fiber orientation changes from 15° to 30°, mode mixity shows a rather significant jump. In the former case, ψ is in the range of −10 to −20°, whereas it ranges from −35° to −50° for $\beta = 45°$ indicating higher K_{II} component and a greater resistance to crack growth at higher angles.

Possible correlation between crack-tip speeds and stress intensity factors are studied in Figure 13. Here both crack speed and stress intensity factor histories are plotted on the vertical axis. It must be noted that crack-tip velocities were computed from smoothed crack extension histories shown in Figure 8. Remarkable match in trends for both these quantities with time for $\beta = 0$, 15, and 30° can be observed once the crack begins to propagate steadily. For $\beta = 45°$, maximum velocity occurs 20–30 μs after the peak value of stress intensity factor is attained. Hence, one could empirically conclude that, for lower fiber orientation angles up to 30°, it seems that crack-tip velocities show good correlation with effective stress intensity factors.

Lastly, it is also instructive to compare stress intensity factors at initiation for all the four cases of β. As expected, stress intensity factor at initiation increases with increasing fiber orientation angle as shown in Figure 14. In this case, stress intensity factors are plotted as a function of E_{xx}/E_{yy} ratio, also known as the degree-of-anisotropy. Stress intensity factor decays exponentially with increasing degree-of-anisotropy, implying that stress intensity factor increases rapidly with increasing β. Parhizgar et al. [8] reported a similar result for quasi-static fracture using compact tension specimens made of glass fiber/epoxy system. Rowlands [9] also reported increasing critical stress intensity factor with increasing angle, but the trend was not an exponential variation possibly due to the multi-directional composite laminates he has studied.

The critical values of stress intensity factors in this study are compared with the ones found in the literature for unidirectional graphite/epoxy composite system in Table 3. Also

[4]The magnitude of stress intensity value could be different if elastic constants measured under dynamic loading condition were used. Although the properties for the material under dynamic loading were not measured in this work, the trends reported by Daniel et al. [29] can be adopted. Since the strain rate used in the current work is close to 'intermediate rate' in [29], similar increases in properties can be reasonably assumed. In [29], E_1 and E_2 increase by 6 and 76%, respectively, and G_{12} and ν_{12} remain unchanged. With this increase, E_1 and E_2 for the current material are expected to be 182 and 14.5 GPa, respectively. These values would increase stress intensity factors accordingly.

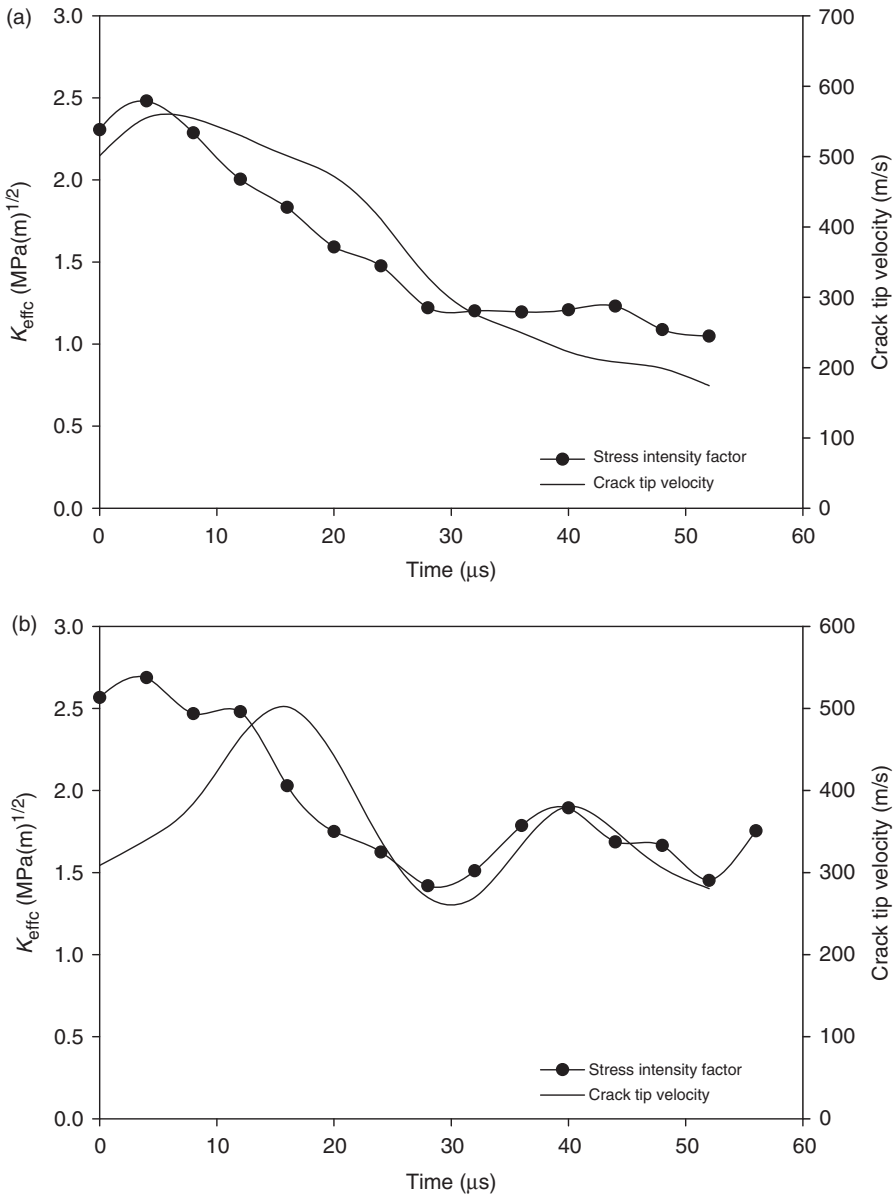

Figure 13. *Effective stress intensity factor in comparison with the crack-tip velocity: (a) $\beta = 0^\circ$, (b) $\beta = 15^\circ$, (c) $\beta = 30^\circ$, (d) $\beta = 45^\circ$ (Horizontal axis denotes time after crack initiation).*

shown are the values obtained using optimally positioned strain gages near the crack-tip during this work independently based on the method suggested in [19]. The difference in values can be attributed to differences in methodology, material systems, loading rates, and/or testing environment. Evidently, the present results compare rather well with those in the earlier studies.

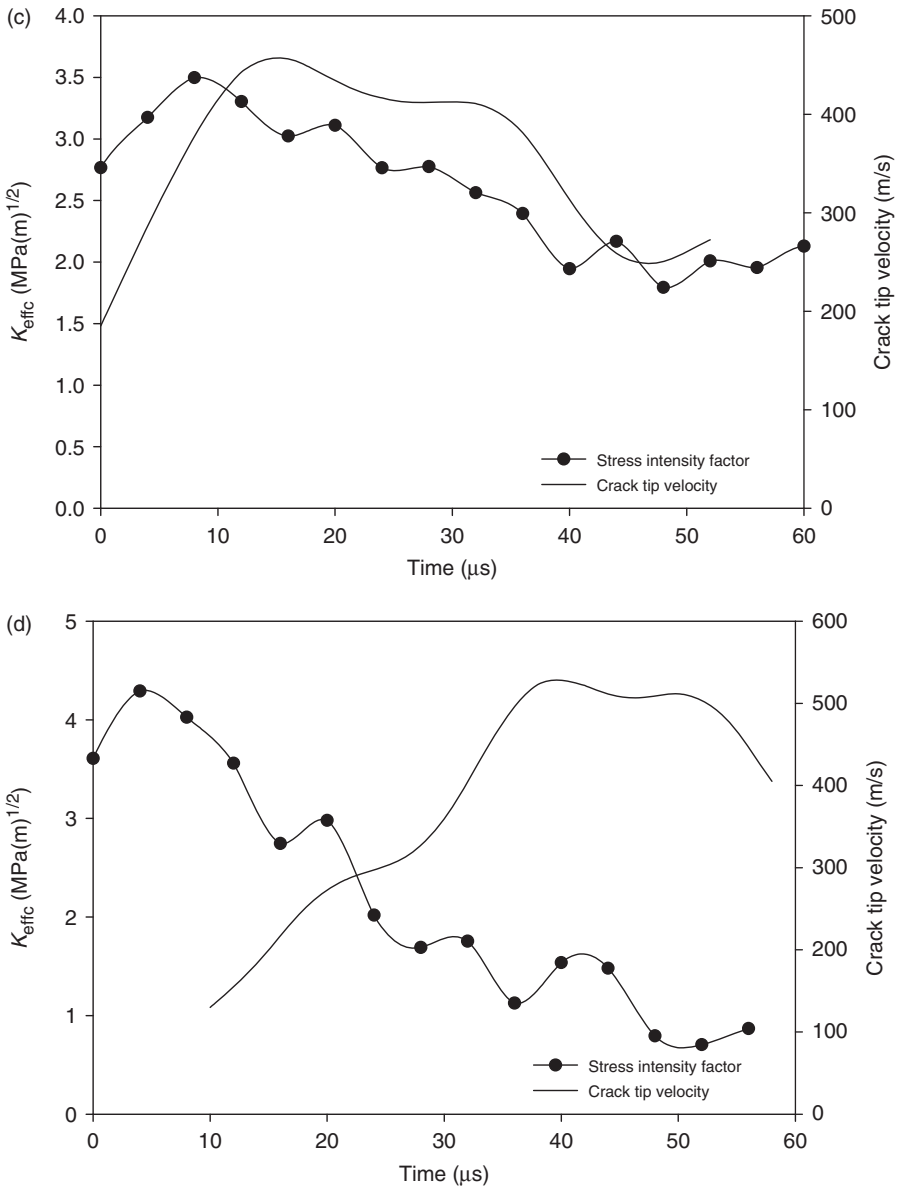

Figure 13. *Continued.*

CONCLUDING REMARKS

The optical technique of DIC coupled with high-speed photography is shown to be effective for characterizing stress-wave induced fracture of unidirectional composite laminates. High-speed photography using a rotating mirror-type digital camera enables locating instantaneous crack-tip positions during a dynamic fracture event and for determining crack growth behavior. The optical method serves to determine full-field information on

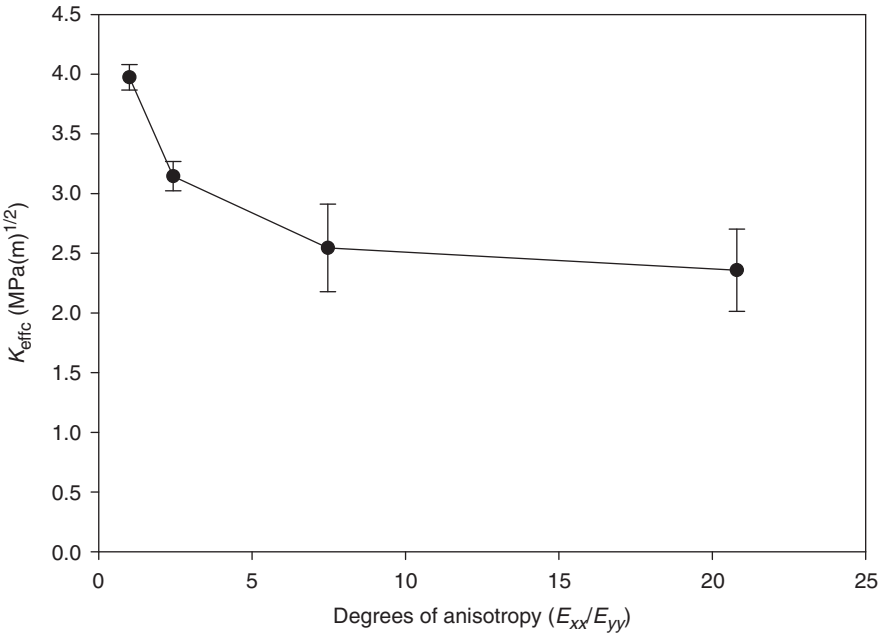

Figure 14. *Effective stress intensity factor as a function of degree-of- anisotropy (E_{xx}/E_{yy}). Due to uncertainty of crack initiation time, standard deviation indicated by error bars is computed from three different values including one image before and one image after crack initiation.*

Table 3. Critical tress intensity factor (K_{Ic}) of various graphite/epoxy systems for $\beta = 0°$.

	Material type	Static[a]	Dynamic[a]
Image correlation	T800/3900-2		2.36
Strain gage	T800/3900-2	1.52	2.01
Ref. [3]	T300/1034C	0.96	
Ref. [5]	IM7/8551-7		1.25
Ref. [31]	IM7/8551-7	1.80	
Ref. [7]	IM7/8551-7	2.30	
Ref. [7]	AS4/3501-6	1.90	
Ref. [12]	Not specified	1.86	
Ref. [30]	Not specified		2.31

[a]Units in MPa$\sqrt{m}$.

deformations in the vicinity of a dynamically growing crack-tip which can be used for estimating fracture parameters. Over-deterministic least-squares analysis of radial displacement components provides stress intensity factors which are in good agreement with the ones from finite element analysis.

The graphite/epoxy laminates show differences in fracture responses depending upon the fiber orientation relative to the initial crack and loading directions. The maximum crack speed observed is the highest for mode-I dominant conditions and it decreases with fiber orientation β. With increasing β, crack takes longer to attain the maximum speed

upon initiation. The effective stress intensity factor K_{eff} at crack initiation increases with β. Alternatively, it is shown to decrease with the degree-of-anisotropy. Changes in crack-tip shear deformations with β, measured in terms of crack-tip mode-mixity, are attributed to these differences. A rather good agreement between the crack initiation values of K_{eff} and the ones from other methods and previous investigations is noted. Lastly, there is a good empirical correlation between dynamic stress intensity factor and crack-tip velocity histories for shallow fiber orientations of $\beta = 0$, 15, and 30°.

ACKNOWLEDGMENTS

This research was sponsored by NASA Langley Research Center under a Grant/Cooperative Agreement (NNX07AC64A) with Auburn University, AL.

REFERENCES

1. Kutyinov, V.F. and Ionov, A.A. (1996). Specific Features of Composite-material Structural Design, In: Zagainov, G.I. and Lozino-Lozinski, G.E. (eds), *Composite Materials in Aerospace Design*, pp. 1–117, Chapman & Hall, London, New York.
2. Tirosh, J. (1980). The Mixed Mode Fracture of Unidirectional Fibrous Composites, *Engineering Fracture Mechanics*, **13**: 119–127.
3. Donaldson, S.L. (1985). Fracture Toughness Testing of Graphite/Epoxy and Graphite/Peek Composites, *Composites*, **16**(2): 103–112.
4. Seif, M.A. and Shahjahun, M. (2001). Mixed-mode Failure of Graphite/Epoxy Composites, *Journal of Engineering Materials and Technology (Transactions of the ASME)*, **123**: 371–376.
5. Liu, C., Huang, Y., Lovato, M.L. and Stout, M.G. (1997). Measurement of the Fracture Toughness of a Fiber-reinforced Composite Using the Brazilian Disk Geometry, *International Journal of Fracture*, **87**(3): 241–263.
6. Yum, Y.J. and Hong, C.S. (1991). Stress Intensity Factors in Finite Orthotropic Plates with a Crack under Mixed Mode Deformation, *International Journal of Fracture*, **47**(1): 53–67.
7. Tohgo, K., Wang, A.S.D. and Chou, T.-W. (1993). A Criterion for Splitting Crack Initiation in Unidirectional Fiber-reinforced Composite, *Journal of Composite Materials*, **27**(11): 1054–1076.
8. Parhizgar, S., Zachary, L.W. and Sun, C.T. (1982). Determination of Fracture Toughness of Unidirectionally Fiber-reinforced Composites, *Fracture of Composite Materials*, In: *Proceedings of the 2nd USA-USSR Symposium*, pp. 215–230, Martinus Nijhoff Publ, Hague, The Netherlands.
9. Rowlands, R.E. (1985). Fracture of Anisotropic and Composite Materials, In: *AMD Symposia Series*, American Society of Mechanical Engineers, Applied Mechanics Division, ASME, New York, NY, Vol. 74, pp. 15–31.
10. Sarkar, P.K. and Maiti, S.K. (1989). Prediction of Mode I Fracture Toughness of Unidirectional Fibre Composites with Arbitrary Crack-fibre Orientation from its Lowest or Matrix-fracture Toughness, *International Journal of Fracture*, **40**(4): R91–R96.
11. Suresh, N. and Wang, A.S.D. (1995). Stress and Energy Based Fracture Conditions for Fiber-wise Splitting in Composites, In: Martin, R.H. (ed.), *Composite Materials: Fatigue and Fracture*, Vol. 5, pp. 176–185, ASTM STP 1230, American Society for Testing and Materials, Philadelphia.
12. Walker, C.A. and Jamasri (1995). Mixed-mode Stress Intensity Factors in Finite, Edge-cracked Orthotropic Plates, *Journal of Strain Analysis for Engineering Design*, **30**(2): 83–90.
13. Kirugulige, M.S., Tippur, H.V. and Denney, T.S. (2007). Measurement of Transient Deformations Using Digital Image Correlation Method and High-speed Photography, *Applied Optics*, **46**(24): 5083–5096.

14. Kirugulige, M.S. and Tippur, H.V. (2009). Measurement of Surface Deformations and Fracture Parameters for a Mixed-mode Crack Driven by Stress Waves Using Image Correlation Technique and High-speed Photography, *Strain*, **45**(2): 108–122.
15. Peters, W.H. and Ranson, W.F. (1982). Digital Imaging Technique in Experimental Stress Analysis, *Optical Engineering*, **21**(3): 427–431.
16. Bruck, H.A., McNeill, S.R., Sutton, M.A. and Peters, W.H. (1989). Digital Image Correlation Using Newton-raphson Method of Partial Differential Correction, *Experimental Mechanics*, **29**(3): 261–268.
17. Chao, Y.-J., Luo, P.F. and Kalthoff, J.F. (1998). An Experimental Study of the Deformation Fields Around a Propagating Crack-tip, *Experimental Mechanics*, **38**(2): 79–85.
18. Sih, G.C., Paris, P.C. and Irwin, G.R. (1965). On Cracks in Rectilinearly Anisotropic Bodies, *International Journal of Fracture Mechanics*, **1**(3): 189–203.
19. Khanna, S.K. and Shukla, A. (1994). Development of Stress Field Equations and Determination of Stress Intensity Factor during Dynamic Fracture of Orthotropic Composite Materials, *Engineering Fracture Mechanics*, **47**(3): 345–359.
20. Piva, A. and Viola, E. (1988). Crack Propagation in an Orthotropic Medium, *Engineering Fracture Mechanics*, **29**(5): 535–548.
21. Chen, D.J., Chiang, F.P., Tan, Y.S. and Don, H.S. (1993). Digital Speckle-displacement Measurement Using a Complex Spectrum Method, *Applied Optics*, **32**(11): 1839–1849.
22. Morozov, V.A. (1993). *Regularization Methods for Ill-Posed Problems*, CRC Press, Ann Arbor, Michigan.
23. Reinsch, C.H. (1967). Smoothing by Spline Functions, *Numerische Mathematik*, **10**: 177–183.
24. Yoneyama, S., Morimoto, Y. and Takashi, M. (2006). Automatic Evaluation of Mixed-mode Stress Intensity Factors Utilizing Digital Image Correlation, *Strain*, **42**(1): 21–29.
25. Sanford, R.J. (1980). Application of the Least-squares Method to Photoelastic Analysis, *Experimental Mechanics*, **20**(6): 192–197.
26. Huang, Y., Wang, W., Liu, C. and Rosakis, A.J. (1999). Analysis of Intersonic Crack Growth in Unidirectional Fiber-reinforced Composites, *Journal of the Mechanics and Physics of Solids*, **47**(9): 1893–1916.
27. Coker, D. and Rosakis, A.J. (2001). Experimental Observations of Intersonic Crack Growth in Asymmetrically Loaded Unidirectional Composite Plates, *Philosophical Magazine A: Physics of Condensed Matter, Structure, Defects and Mechanical Properties*, **81**(3): 571–595.
28. Gilat, A., Goldberg, R.K. and Roberts, G.D. (2002). Experimental Study of Strain-rate-dependent Behavior of Carbon/Epoxy Composite, *Composites Science and Technology*, **62**(10–11): 1469–1476.
29. Daniel, I.M., Hamilton, W.G. and LaBedz, R.H. (1982). Strain Rate Characterization of Unidirectional Graphite/Epoxy Composite, In: Daniel, I.M. (ed.), *Composite Materials: Testing and Design (6th Conference)*, pp. 393–413, ASTM STP 787, American Society for Testing and Materials, Philadelphia.
30. Lambros, J. and Rosakis, A.J. (1997). Dynamic Crack Initiation and Growth in Thick Unidirectional Graphite/Epoxy Plates, *Composites Science and Technology*, **57**(1): 55–65.
31. Liu, C., Rosakis, A.J., Ellis, R.W. and Stout, M.G. (1998). A Study of the Fracture Behavior of Unidirectional Fiber-reinforced Composites Using Coherent Gradient Sensing (CGS) Interferometry, *International Journal of Fracture*, **90**(4): 355–382.